J. Fluid Mech. (2007), *vol.* 572, *pp.* 287–310. © 2007 Cambridge University Press
doi:10.1017/S0022112006003612 Printed in the United Kingdom

The reopening of a collapsed fluid-filled elastic tube

By ANNE JUEL AND ALEXANDRA HEAP
School of Mathematics, The University of Manchester, Manchester M13 9PL, UK
anne.juel@manchester.ac.uk

(Received 27 October 2005 and in revised form 14 July 2006)

We present an experimental study of the reopening mechanics of a collapsed liquid-filled elastic tube. The experiment is a simple mechanical model of pulmonary airway reopening and aims to assess the robustness of existing theoretical models. A metre-long horizontal elastic tube of inner radius $R_i = 4.88 \pm 0.14$ mm is filled with silicone oil and is carefully collapsed mechanically. The injection of nitrogen at a constant flow rate results in the steady propagation of an air finger, after the decay of initial transients. This behaviour is observed over the realizable range of the capillary numbers *Ca*, which measures the ratio of viscous and capillary forces. With increasing *Ca*, the transition region between the collapsed and reopened sections of the tube shortens, and the height of the tube behind the bubble tip increases. We also find that air fingers can propagate in partially reopened tubes, in which the transmural pressure is negative far behind the finger tip.

The effect of viscosity on the reopening dynamics was explored by performing experiments using three different grades of silicone oil, with kinematic viscosities of 1000 cS, 200 cS and 100 cS. A direct comparison between the experimental pressure dependence on *Ca* and numerical simulations of the zero-gravity three-dimensional airway-reopening model of Hazel & Heil (*Trans. ASME*: *J. Biomech. Engng*, vol. 128, 2006, p. 473) highlights some significant differences. Within the experimental parameter range, gravity profoundly influences the reopening mechanics in several ways. The reopening tube is supported by a rigid base, which induces an asymmetry about the horizontal mid-plane of the collapsed tube, resulting in distinct phases of reopening as *Ca* increases. In addition, buoyancy forces act on the air finger, which is observed to propagate near the top of the cross-section of the tube, leaving a thicker fluid-lining below. In the limit of small *Ca*, the height of the reopened tube increases significantly with viscosity. Experimental evidence suggests that this increase in viscosity leads to significant changes in the film configuration behind the propagating finger, caused by the increased contribution of buoyancy forces. The altered film configuration changes the mechanical load on the tube walls and, hence, the shape of the reopened tube.

1. Introduction

The airways of the lungs form a branched network of fluid-lined elastic vessels linking the trachea to the alveoli, where gas exchange takes place. A number of pulmonary conditions are known to trigger the collapse of the smaller airways (Perun & Gaver III 1995*b*; Grotberg 2001). The collapse may occur through a fluid-elastic instability, which causes the tube to buckle and eventually leads to a configuration in which a liquid bridge occludes the airway (Kamm & Schroter 1989; Halpern & Grotberg

1992; White & Heil 2005; Hazel & Heil 2005). Once collapsed, the airway must be reopened quickly with minimal damage to the lining tissues. When long sections are occluded, reopening is believed to occur through the propagation of an air finger (Macklem, Proctor & Moss 1970; Naureckas *et al.* 1994). Thus, in the last 15 years, significant efforts have been focused on understanding the mechanics of this process.

The first experimental model of airway reopening, by Gaver III, Samsel & Solway (1990), comprised a thin-walled polyethylene tube that was mechanically collapsed to a ribbon-like configuration and contained a thin liquid film to hold the walls in apposition. An air finger was injected at constant pressure and propagated in an approximately steady fashion by 'peeling' apart the walls. The tube had minimal bending stiffness and the fluid–structure interaction arose essentially through the large tension imposed on the end of the tube, relative to the viscous and capillary forces inside the tube. The radius of the tube, R, was identified as the dominant length scale and the dimensionless bubble pressure, $P = P^* R/\sigma^*$, was found to scale approximately linearly with the capillary number, $Ca = \mu U/\sigma^*$; here P^* denotes the dimensional bubble pressure (the pressure of the air finger relative to the external pressure), U the propagation speed of the air finger, μ the dynamic viscosity of the lining fluid and σ^* the surface tension at the air–liquid interface. The capillary number is a measure of the viscous forces relative to the capillary forces in the system and provides a non-dimensional measure of the propagation speed of the finger. Gaver III *et al.* (1990) also demonstrated the existence of a yield pressure, $P_y^* \sim 8\sigma^*/R$, as $Ca \rightarrow 0$, which must be exceeded for an air finger to propagate.

A subsequent study by Perun & Gaver III (1995*a*) concentrated on a two-dimensional analogue of this experiment, where both the collapsed and reopened ends of the airway were constrained to a planar configuration. The results of this study were qualitatively similar to those of Gaver III *et al.* (1990), although the airway geometry was found to influence the bubble pressures significantly. For air injected at a constant flow rate, the pressure of reopening was observed to reach a steady state for $Ca > 0.5$, following a short unsteady transient. Increasingly unsteady reopening processes were observed for $Ca < 0.5$. Furthermore, the yield pressure was reduced by a factor of approximately 2 compared with that estimated by Gaver III *et al.* (1990). Additionally, the effect of tethering was addressed by Perun & Gaver III (1995*b*), who found that the asymmetric loading on the tube caused a change in the reopening pressures. Experiments with non-Newtonian fluids by Low, Chew & Zhou (1997) revealed that the presence of a yield stress leads to increased yield pressures and reopening times.

Gaver III *et al.* (1996) proposed a two-dimensional theoretical model for the experiments of Perun & Gaver III (1995*b*). Using a combination of a lubrication analysis and the boundary-element method, they considered the propagation of an air finger into a fluid-filled channel whose flexible walls were placed under tension and supported by linearly elastic springs. Their analysis showed a two-branch behaviour in the P–Ca relationship. For low Ca, the 'pushing branch' results from the coupling between surface tension and elastic stresses, P decreasing as Ca increases. In the high-Ca limit, the 'peeling branch' results from the balance between viscous and longitudinal wall tension forces, and P increases monotonically with Ca. Two-dimensional airway reopening was also addressed by Jensen *et al.* (2002), whose asymptotic analysis relied on the assumption that the membrane slope is uniformly small, so that the bubble pressures could be predicted analytically over a wide range of Ca. A comparison between the experimental measurements of Perun & Gaver III (1995*b*) and boundary-element simulations of an asymmetric tube with a symmetrically separated liquid layer yielded good agreement to within 10 % over the peeling branch. The reopening pressures obtained numerically for the asymmetric tube were a factor of approximately 1.6 larger than in the symmetric case. The effect of inertial forces on the reopening dynamics was addressed numerically by Heil (2000) using a finite-element method. Inertial forces were quantified by the speed-independent parameter $Re/Ca = \rho\,\sigma^* R/\mu^2$, where $Re = \rho\,U\,R/\mu$ is the Reynolds number and ρ is the density of the liquid. In the presence of finite bending stiffness of the walls, Heil found that even for relatively small Re/Ca, i.e. values between 5 and 10, the transition region of the reopening tube is significantly altered, resulting in steepening of the P–Ca curves. Finally, a detailed study of the physiologically relevant influence of surfactant was performed recently by Naire & Jensen (2005).

A fundamental shortcoming of some two-dimensional models is that a change in transmural pressure is equivalent to a rescaling of the transverse length scale, unless the use of a nonlinear tube law provides a natural length scale (Naire & Jensen 2005). Thus Hazel & Heil (2003) developed a three-dimensional numerical model of airway reopening in which the radius of the tube provides a natural transverse length scale, so that the transmural pressure becomes a significant variable of the system. They considered the steady motion of an inviscid air finger reopening a fluid-filled collapsed elastic tube of infinite length by coupling nonlinear Kirchhoff–Love shell theory to the free–surface Stokes equations. The level of fluid-structure interaction was measured by the non-dimensional surface tension, $\sigma = \sigma^*/(RK)$, which corresponds to the ratio of capillary and elastic forces; K is the bending stiffness of the tube. The initial level of tube collapse was characterized by the reduced cross-sectional area, $A_\infty = A^*_\infty/(4R^2)$, where A^*_∞ is the dimensional cross-sectional area of the tube far ahead of the bubble. This model of airway reopening was developed in the limit of zero gravity, so that the fluid lining left behind the advancing finger on the tube walls retained the up–down symmetry of the cross-section. Thus, far behind the finger tip, the tube reopened approximately according to the cross-sectional shapes predicted by the ‘tube law’ (Shapiro 1977). The qualitative behaviour of the system was found to be very similar to the two-dimensional predictions of Gaver III *et al.* (1996) and Heil (2000), with a two-branch behaviour of the P–Ca relationship. The pressure required to drive the finger at a given speed was found to increase with both σ and A_∞, so that higher-pressure bubbles were required to reopen less strongly collapsed tubes. If σ were sufficiently small, steady airway reopening could occur for pressures lower than the external (pleural) pressure, i.e. the airway remained buckled after the passage of the air finger. This is the limit investigated in the present experiments.

Hazel & Heil (2006) recently extended the three-dimensional Stokes model to finite Reynolds numbers, so that the air-finger propagation was governed by Re, Ca, σ and A_∞. They showed that, as in the two-dimensional model of Heil (2000), inertial forces have a significant effect on the bubble pressures, strongly influencing the fluid dynamics and wall shape in the vicinity of the advancing finger tip, through a mechanism consistent with the Bernoulli effect.

Thus far, airway reopening in tubes of significant bending stiffness has been addressed exclusively by theoretical and numerical studies and, invariably, the models are based on several approximations, for instance, steady-state propagation and zero gravity (Hazel & Heil 2003, 2006). As reported in this paper, we chose to perform a detailed laboratory investigation of the mechanics of airway reopening, which enabled us to assess the robustness of these theoretical approximations. In addition to the fluid parameters Ca and Re, the presence of gravity forces can be quantified relative to the capillary forces by the Bond number, $Bo = \rho\,g\,R^2/\sigma^*$. We chose the mid-wall radius, $R = R_i + h/2$, where R_i is the inner radius and h the wall thickness of the tube, as the experimental length scale. Our experimental setup is described in § 2.1, with a strong emphasis on experimental control and reproducibility. We focus on a simple laboratory model of air-finger propagation in a long, horizontal, fluid-filled, partially collapsed tube. In contrast with the earlier experiments of Gaver III *et al.* (1990), where the large tension applied to the end of the tube dominated the fluid–structure interaction and the small bending stiffness of the polyethylene tube played a negligible role, our elastic silicone tube was chosen for its finite bending stiffness, with $\sigma = 3.6 \times 10^{-2}$. This yields ratios of viscous and elastic forces $\sigma\, Ca$ of up to 0.4, a significant fluid–structure interaction. Our value of σ, however, is much smaller than estimates for the deep lung of approximately $\sigma = 50$ (Hazel & Heil 2003), and thus a direct comparison with pulmonary behaviour should be made with caution. The low value of σ results in airway-reopening pressures that are largely negative, in contrast with the experiments of Gaver III *et al.* (1990) and Perun & Gaver III (1995*a*,*b*). The tube collapses with two-fold symmetry according to a classical 'tube law', which, as reported in § 2.2, we measured in order to determine the value of the dimensional bending stiffness of the tube. Thus, our experiment models an idealized isolated airway and, in the interest of simplicity, we neglect tethering and do not add surfactants, although both are important in the lung.

The effect of viscosity on the reopening dynamics is explored in § 3 by presenting experiments using three different grades of silicone oil, with kinematic viscosities of 1000 cS, 200 cS and 100 cS. We attempt a direct comparison between the experimental pressures and the computational results of Hazel & Heil (2006) in § 3.1, which highlights significant differences in the P–Ca relationship. We attribute these differences to the presence of gravity in the experiment, whose dual effect on the reopening mechanics is discussed in § 3.2. In essence, buoyancy affects the level of reopening behind the finger tip through changes to the flow configuration inside the tube, while gravity acting on the reopening tube breaks the symmetry of the transition region, which results in distinct phases of reopening with increasing Ca.

2. Experimental methods

2.1. *Description of the apparatus and experimental procedure*

A schematic diagram of the experimental apparatus is shown in figure 1. The working part of the apparatus consisted of a piece of translucent extruded silicone tubing (Primasil Silicones Ltd) 1.0 m long positioned on a solid base plate. The tubing had an inner radius $R_i = 4.88 \pm 0.14$ mm and wall thickness $h = 0.48 \pm 0.07$ mm. The downstream end was connected to a two-way valve, which was operated manually. At the upstream end, a three-way pneumatic solenoid valve was used to switch the gas flow from exiting into the atmosphere to entering the tube at the start of each experiment.

The flow source was a compressed nitrogen cylinder, whose flow rate was controlled by a fine needle valve and was accurately monitored using a 0–5000 $\mathrm{cm^3\,min^{-1}}$ mass-airflow meter (AWM5000 microbridge mass-airflow sensor, Honeywell) to range between 50 and 1400 $\mathrm{cm^3\,min^{-1}}$. The air-mass flow meter was powered by a 10.000 ± 0.001 V stabilised direct current supply and readings were made with a five-digit-accuracy voltmeter. At 1400 $\mathrm{cm^3\,min^{-1}}$, the Reynolds number of the air jet flowing out of the solenoid valve nozzle into the tube was approximately equal to 340. Beyond this value the recorded pressure traces showed increasing levels of fluctuations, believed to be due to instabilities in the injected air. A differential pressure sensor (Honeywell, $\pm 5''\,\mathrm{H_2O}$) was attached to the line immediately upstream of the solenoid valve, via

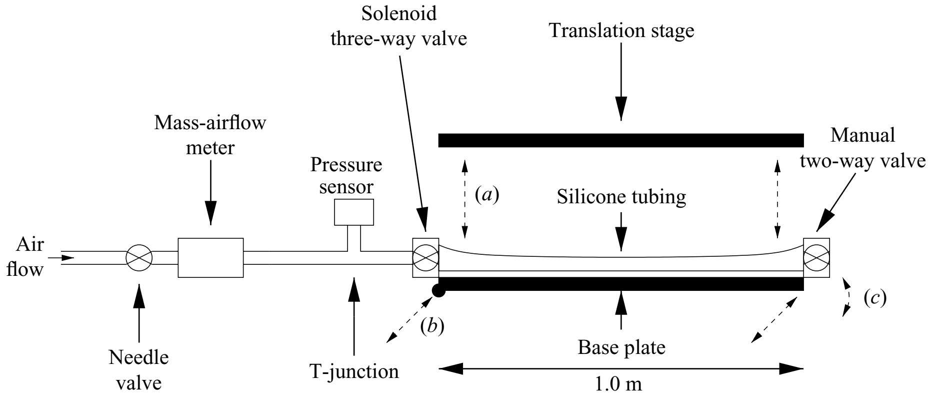

FIGURE 1. Schematic diagram of the experimental apparatus. (*a*) The vertical dashed arrow shows motion of the upper plate; (*b*) the diagonal dashed arrows show the horizontal motion of the support plate; (*c*) the curved arrow at the night shows the 25° tilt of the support plate.

a T-junction connected to one of its ports, while the second port of the pressure sensor was left open to the atmosphere. The pressure sensor was powered by the same power supply as the mass-airflow meter and was calibrated *in situ* against a water-filled U-tube manometer. The bubble pressure in the elastic tube was obtained by subtracting from the sensor measurements the small pressure drop due to the rigid gas line between the sensor and the inlet of the flexible tube, which was measured for an open circuit. The pressure was sampled on a personal computer via an RS232 serial connection from a high-resolution voltmeter at a rate of 25 Hz.

In addition to the pressure measurements, two analogue CCD cameras were used to monitor the reopening process, as shown in figure 2. One camera captured a side view of the tube over a length of 13 cm, starting at least 50 cm downstream of the inlet. Its position was chosen, depending on the flow rate, to ensure that all transient behaviour had decayed. It was used to record the propagation speed of the air bubble reopening the tube and also to capture images of the transition region between the collapsed and reopened sections of the tube. In order to obtain a quantitative measure of the deformation of the top half of the tube, a laser sheet was shone onto the tube at an angle of 50° from the vertical and the second camera was placed vertically above the illuminated region to provide a top view of a section of the tube approximately 2.5 cm long by 2.0 cm wide. As shown schematically in figure 2, the laser sheet illuminated the tube wall at different horizontal positions depending on the local height of the tube, thus outlining local deformations relative to the horizontal base plate. The local height of the tube was given by $D = d/\tan 50°$, where d is the displacement of the laser line from its position on the flat base plate. An example of the aerial visualization is shown in figure 3, where the laser line outlines the deformation of the top half of the collapsed tube. The images of the two cameras were combined using an image inserter (Kramer, PIP-200) and sampled simultaneously onto a personal computer at a rate of 25 frames s^{-1}. The resolutions of the side and aerial-view images were 0.18 and 0.09 mm per pixel respectively. The values of the maximum height of the tube were the same, within the experimental resolution, when measured with the aerial and side-view cameras.

The base plate, on which the tube and valves were positioned, was accurately levelled and its vertical position was held fixed. It was mounted rigidly beneath a facing parallel plate on a vertical translation stage whose purpose was to collapse the

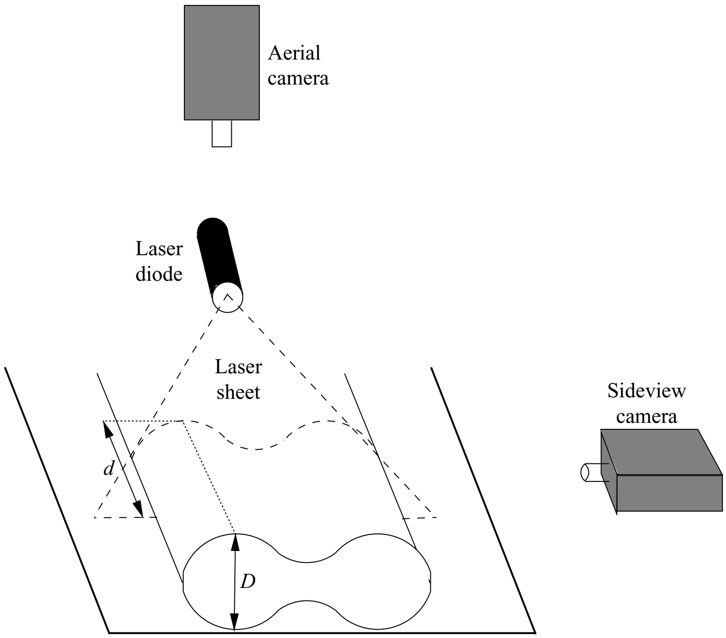

FIGURE 2. Schematic diagram of the visualisation setup. A laser sheet, oriented at 50° from the vertical, is shone onto the deformed tube. The tube is illuminated at different horizontal positions depending on its local height. Thus, the laser sheet outlines local deformations relative to the horizontal base plate, which are captured by the aerial camera. A sideview camera monitors the reopening process over a section of tube 13 cm long.

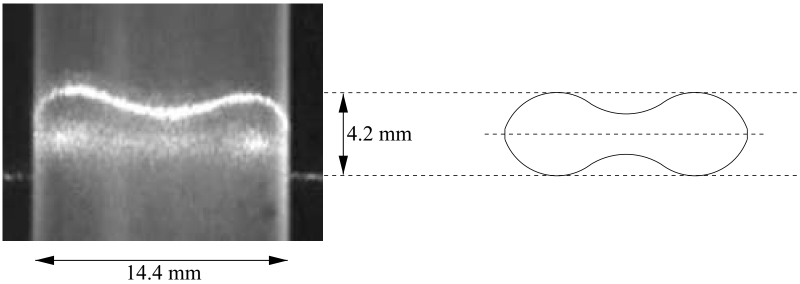

FIGURE 3. Aerial view of the collapsed liquid-filled tube prior to an experimental run. The experimental visualization technique, depicted in figure 2, provides a quantitative measure of the outline of the top half of the deformed tube. The schematic diagram on the right-hand side depicts the full cross-sectional area of the collapsed tube, under the assumption of a symmetric collapsed cross-section.

tube mechanically prior to an experiment, as shown in figure 1. The base plate was mounted on bearings so that it could slide forward from under the main frame to facilitate the filling of the tube. It was hinged at the upstream end so that it could be tilted upward by 25°, and supported by a hinged arm at the downstream end. The tube was then slowly filled with liquid via the downstream two-way valve. This method eliminated any handling of the tube during the experimental process and allowed all air bubbles to rise and be expelled.

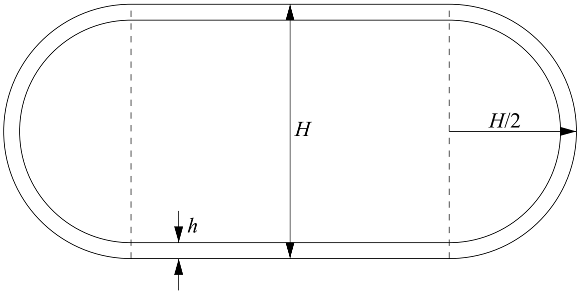

FIGURE 4. Schematic diagram of the strained shape adopted by the cross-section of the tube, after collapse but while still in contact with both plates. This shape can be closely approximated by a rectangle of height H capped by two semicircles, each of radius $H/2$.

Silicone oil grade (cS)	μ (kg m^{-1}s^{-1})	ρ (kg m^{-3})	σ^* (N m^{-1})	$Re/Ca = \rho\sigma^* R/\mu^2$
100	0.111	961	2.04×10^{-2}	8.2
200	0.216	962	2.05×10^{-2}	2.2
1000	1.065	966	2.07×10^{-2}	0.1

TABLE 1. Physical properties of the silicone fluids at 18 °C, where μ denotes the dynamic viscosity, ρ the density and σ^* the surface tension with air. The ratio of the Reynolds number and the capillary number, Re/Ca, is also given for each fluid.

After the filling procedure, the base plate was returned to its initial position so that the silicone tube could be collapsed. This was achieved mechanically by lowering the upper plate onto the liquid-filled tube while carefully letting the excess liquid escape through the downstream valve. The position of the upper plate could be adjusted to within 0.02 mm, which was less than 1 % of the height of the collapsed tube. Hence, the height of the collapsed tube H could be uniformly and reproducibly attained. All the experiments presented in this paper were conducted with tubes collapsed to a height $H = 2.92 \pm 0.02$ mm, which corresponds to a reduction of 73 % from the undeformed state. During this mechanical collapse the cross-section of the tube adopted a strained shape, which could be closely approximated by a rectangle of height H capped by two semicircles, each of radius $H/2$, as shown in figure 4. After the collapse was completed, the downstream valve was closed and the upper plate was lifted off the tube. The tube then relaxed into its equilibrium shape, which consisted of two end lobes separated by a thinner central region, as shown schematically in figure 3. Here, we have assumed that the collapsed cross-section is symmetric, although the top-view visualization yields measurements of only the top half-section of the tube.

The working liquid was silicone oil, which was chosen for its stable interfacial properties and because it fully wets the tube. Experiments were carried out with oils of three different viscosities. The experiments were conducted in a temperature-controlled room at $18 \pm 1°$ C; the physical properties of the oils at this temperature are given in table 1. The dynamic viscosity μ and the density ρ were measured in the laboratory and the value of the surface tension σ^* was determined on the basis of the the manufacturer's data and the temperature coefficient of surface tension quoted by Schatz *et al.* (1995) for silicone oil.

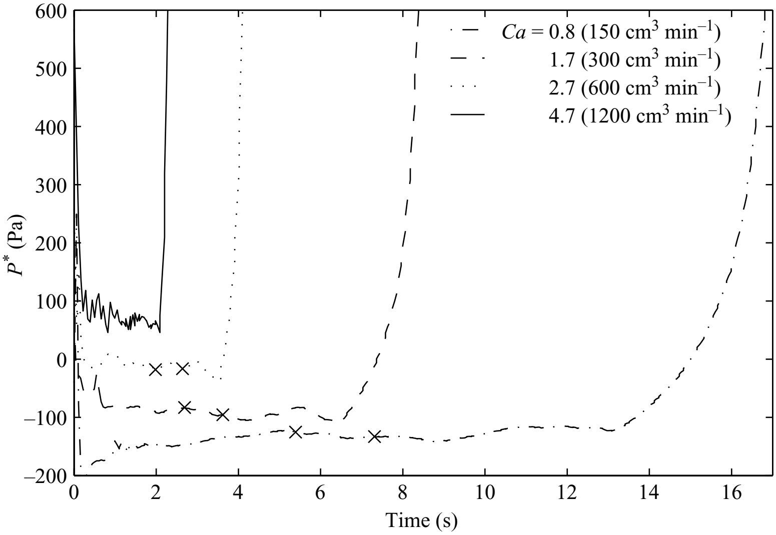

FIGURE 5. Pressure time series measured for 150, 300, 600 and 1200 cm^3 min^{-1}, with 200 cS silicone oil. In each case, the approximately constant pressure trace that follows short initial transients linked to the switching of the solenoid valve indicates the steady propagation of an air finger. The pairs of markers on each curve delimit the region in which the propagating air finger is captured by the side-view camera. An average pressure value is calculated in this interval. The sharp rise in pressure at the end of the experiment corresponds to the time at which the air finger reaches the end of the tube and the associated inflation of the reopened tube takes place. The duration of the experiments reduces with increasing flow rate, because the finger propagates with increasing speed.

Once the tube had been filled and collapsed, the nitrogen flow into the atmosphere was adjusted with the needle valve. The solenoid valve was then triggered to direct the nitrogen flow into the collapsed, liquid-filled, tube and the sampling of both the pressure and video footage was initiated. In most cases, an air finger of approximately constant pressure was observed to propagate steadily down the tube. Four typical pressure traces sampled at flow rates of 150, 300, 600 and 1200 cm^3 min^{-1} with 200 cS silicone oil are shown in figure 5. The steady state was established within approximately 1 s of the opening of the solenoid valve. When the air finger was within approximately 5 cm from the end of the tube the pressure rose rapidly, as the injected flow continued to inflate the reopened tube and saturated the pressure sensor. At this point the experiment was discontinued, by opening the end valve, to avoid permanent deformation of the silicone tube. The pressure of reopening was determined by averaging the recorded pressure trace over the section 13 cm long monitored by the side-view camera, delimited by markers on the pressure traces in figure 5.

2.2. *Experimental parameters and elastic properties of the tubes*

The fluid parameters required to describe the steady propagation of an air finger in the experiment are *Ca*, the ratio of viscous and capillary forces, *Re*, the ratio of inertial and viscous forces and *Bo*, the ratio of gravity and capillary forces. The ratios $Ca = \mu U/\sigma^*$ and $Re = \rho U R/\mu$ depend on the finger speed, which is accurately determined using the side-view images of the reopening tube. The ratio Re/Ca, given in table 1, depends exclusively on the physical properties of the fluids and the radius of the tube, as does $Bo = \rho g R^2/\sigma^* = 12.1$, which remains constant in the experiments.

The cross-sectional area of the collapsed tube, A^*_∞, was calculated by approximating the shape of the cross-section of the tube held between the plates of the translation stage at the end of the collapse procedure by a rectangle capped by two semicircles, as mentioned above (see figure 4). Thus, assuming negligible stretching during the collapse procedure, the circumference of the tube remains constant and the cross-sectional area of the collapsed tube, estimated midway through the wall thickness, is given by

$$A^*_\infty = \pi\left(\frac{H}{2}-\frac{h}{2}\right)^2 + (H-h)\left(\frac{2\pi R - \pi(H-h)}{2}\right),$$

where $R = 5.12\,\mathrm{mm}$ is the midwall radius of the undeformed tube, $h = 0.48\,\mathrm{mm}$ is the wall thickness and $H = 2.92\,\mathrm{mm}$ is the height of the collapsed tube held between the plates of the translation stage. Hence

$$A_\infty = \frac{A^*_\infty}{4R^2} = 0.33$$

for all the experiments presented in this paper.

The final non-dimensional group of parameters involves the elastic properties of the tube; it is the non-dimensional surface tension $\sigma = \sigma^*/(R\,K)$, which measures the relative effect of capillary and elastic forces and requires knowledge of the bending stiffness K of the tube. Using thin-shell theory, Flaherty, Keller & Rubinow (1972) predicted that the pressure of opposite-wall contact in a buckled elastic tube of two-fold symmetry and undeformed circular cross-section, in the absence of gravity, is

$$\frac{P^*_{owc}}{K} = -5.25.$$

A. L. Hazel (2005, personal communication) estimated numerically that the pressure of opposite-wall contact of a silicone ring with $h/R = 0.09$, deforming under its own weight on a rigid surface, is reduced by less than 1.5 % compared with the zero-gravity case. In order to determine the pressure of opposite-wall contact and hence the value of K experimentally, measurements were made of the dependence of the transmural pressure on the cross-sectional area, commonly referred to as the 'tube law'. An empty tube was fully collapsed and slowly reopened by injecting air at a flow rate of $50\,\mathrm{cm}^3\,\mathrm{min}^{-1}$. The tube reopened uniformly along its entire length, suggesting that its cross-sectional area is proportional to the time elapsed since the opening of the solenoid valve. An example of this experimental 'tube law' is shown in figure 6. The dimensional transmural pressure P^*_t is plotted against the cross-sectional area of the tube A normalized by the undeformed cross-sectional area, $A_0 = \pi R_i^2$. The transmural pressure goes through zero slightly below $A/A_0 = 1$. This small discrepancy is due to the effect of gravity, which reduced the inflated height of the tube by less than 5 %. The point of opposite-wall contact is clearly visible as a kink in the curve. The pressure at this point was found to be independent of the flow rate at which the collapsed tube reopened, and measurements performed in four non-contiguous lengths of tube gave $P^*_{owc} = -591 \pm 12\,\mathrm{Pa}$. Thus, the value of the bending stiffness is $K = 112 \pm 2\,\mathrm{N\,m}^{-2}$, and the non-dimensional surface tension has the same value, $\sigma = (3.6 \pm 0.2) \times 10^{-2}$, for all three grades of silicone oil.

2.3. *Experimental reproducibility*

Silicone oil slowly diffuses into the wall of the tubing, altering its elastic properties. In order to minimize this effect, tubes were discarded after six experiments and a system was instigated to check the reproducibility of the results. For each tube used,

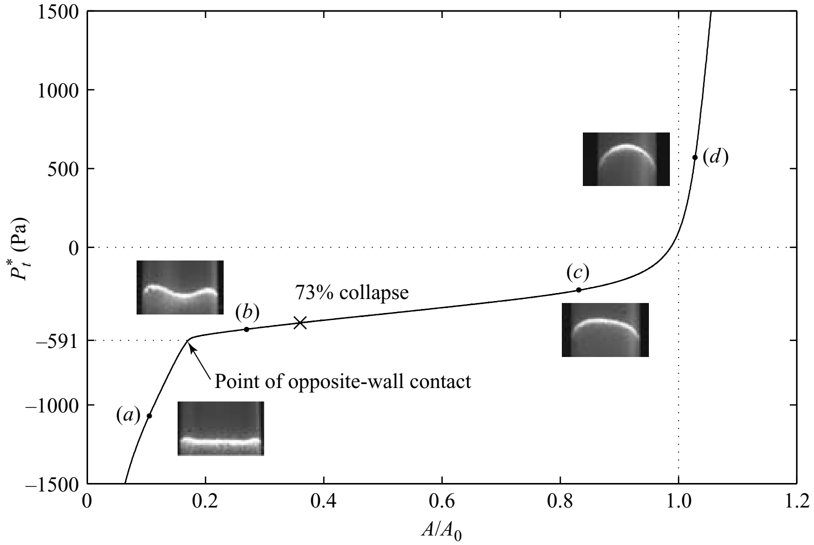

FIGURE 6. Experimental ‘tube law’: dependence of the transmural pressure P_t^* on the cross-sectional area of an empty tube (solid line). The measurements were obtained by fully collapsing an empty tube and subsequently reopening it ‘quasi-statically’ (with air injected at a flow rate of 50 cm^3 min^{-1}). The insets are images of the top half of the tube for different levels of collapse. The laser line outlines the shape of the tube: (*a*) the fully collapsed tube with minimal lobes at the side boundaries; (*b*) the buckled shape near the point of opposite-wall contact, with increasingly large side lobes; (*c*) the buckled tube with approximately elliptical cross-section; (*d*) the inflated tube with circular cross section. The point of opposite-wall contact corresponds to the kink in the curve. The pressure measured at this point is $P_{owc}^* = -591$ Pa. The point of 73 % collapse, which corresponds to the initial level of collapse in the bubble propagation experiments, is highlighted with a marker.

three flow rates were applied and for each flow rate the experiments were conducted twice, the same flow rate being selected for the first and last experiments on a given tube. In addition, rather than monotonically incrementing the flow rate its values were selected randomly, in order to avoid systematic patterns of bubble pressure due to unavoidable fluctuations in the wall thickness along the length of a tube. Finally, in order to ensure a sufficient sample of data, between two and 13 experiments were performed at each flow rate.

An example of a pressure data set gathered at a flow rate of 300 cm^3 min^{-1}, with 200 cS silicone oil, over three experiments is presented in figure 7. Experiments 1 and 2 were conducted with the same tube on the same day, whereas experiment 3 was carried out two weeks later with a different, non-contiguous, section of tube. The comparison between these three pressure traces demonstrates a good experimental reproducibility during the steady-state propagation phase, since the third experimental trace lies between the two traces measured using the same tube. The fluctuations observed in these pressure traces are believed to be due to small variations in wall thickness along the length of the tube, as well as unavoidable perturbations in the ambient pressure. The fluctuations within each set of measurements at a given flow rate are less than 40 Pa. The total pressure range of interest, 400 Pa, is also small, however, so that the experimental error at each flow rate is approximately 10 % of the investigated-pressure range.

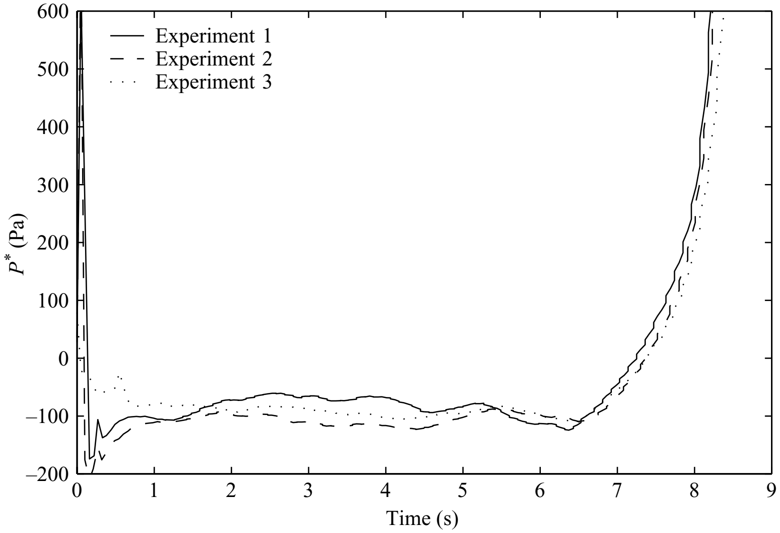

FIGURE 7. Three pressure traces recorded at the same value of the flow rate, $300\,\text{cm}^3\,\text{min}^{-1}$, and with 200 cS silicone oil. Experiments 1 and 2 were performed with the same piece of silicone tubing on the same day. Experiment 3 was carried out two weeks later with a different tube from the same batch.

In addition, the experiments were extremely sensitive to small imperfections in the tubes. The slightly adhesive nature of the silicone created storage difficulties, as the tubes tended to stick together, causing permanent deformations. This issue was resolved by coating the outer walls of the tubes with talcum powder and storing them carefully in a box 1 m long. To probe the sensitivity of the reopening dynamics to imperfections arising during the experimental setup procedure, a minimal twisting strain was introduced prior to one test experiment performed with 200 cS silicone oil at a flow rate of $300\,\text{cm}^3\,\text{min}^{-1}$. A comparison between the resulting pressure trace (the dashed line) and that from an unperturbed experiment (the solid line) is shown in figure 8. The significant variation of the perturbed pressure indicates that the air finger does not propagate uniformly. The perturbed pressure trace exhibits fluctuations of 48 Pa compared with 7 Pa for the normal pressure over the measurement section. This example highlights the quality of experimental control achieved in the results shown in figure 7.

The experiments shown in figure 8 were carried out with a tube from a batch different from the single batch of 150 m of tubing used for the remainder of the experiments presented in this paper. The pressure level during steady finger propagation is approximately −500 Pa, which may be compared with −100 Pa for the experiments shown in figure 7. This significant difference is due to variations in the elastic properties of the silicone rubber as well as changes in the wall thickness between batches, both of which altered the bending stiffness and thus reduced σ by approximately 25 %. These results are in agreement with the computations of Hazel & Heil (2003), which indicate significant reductions in the bubble pressure with decreasing σ, for the small values of σ investigated experimentally.

3. Results

We present experimental results obtained for three different grades of silicone oil, as shown in table 1. A total of 47, 111 and 74 experiments were performed for the

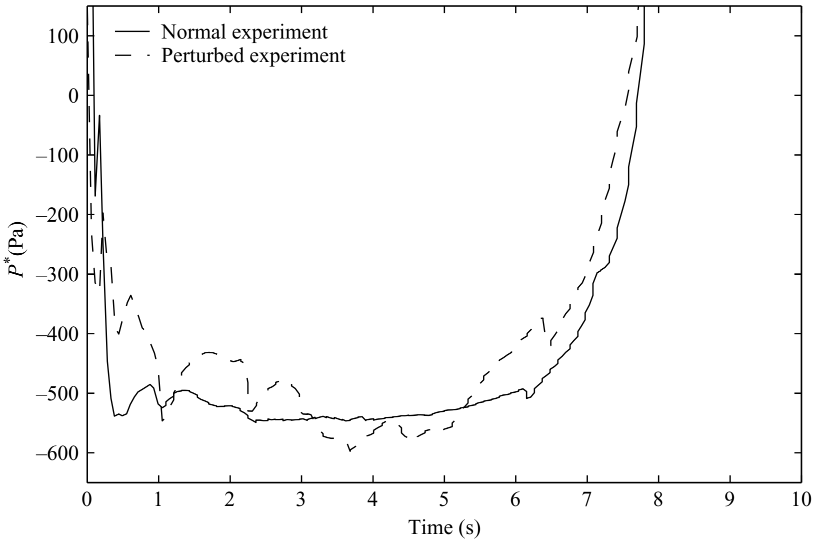

FIGURE 8. Effect of small experimental perturbations on the pressure traces. In the perturbed experiment, a minimal twisting strain was applied to the tube during setup. Both experiments were performed for 300 cm^3 min^{-1} with 200 cS silicone oil. The pressure level during the steady finger propagation is approximately −500 Pa compared with −100 Pa in the experiments shown in figure 7. This difference is due to the use of a tube from a different batch to that used for the remainder of the experiments presented in this paper.

1000 cS, 200 cS and 100 cS silicone oils respectively. Between two and 13 realizations of the experiment were performed at each flow rate, so that significant trends could be reliably extracted in spite of the difficulties associated with the smallness of the pressure range of interest and the unavoidable fluctuations present in the system. For each value of the imposed flow rate, the same (P, Ca) state was detected during each realization of the experiment. Thus we present the results averaged for each flow rate, with upper and lower error bars each corresponding to one standard deviation from the mean of the data set. These error bars are larger than any error estimated from the variations within a single experiment. Particular attention is focused on the 200 cS experiments (there were 111 such experiments, and up to 13 measurements per flow rate), because they exhibited the most complex dynamics.

3.1. *Pressure measurements: comparison with numerical simulations*

The dependence of the bubble pressure on Ca is shown in figure 9 for the three grades of silicone oil investigated. The pressure is non-dimensionalized on the capillary scale, $P = P^* R/\sigma^*$, where P^* is the dimensional bubble pressure (the pressure of the air finger relative to the external pressure). Experimental pressure measurements are shown by symbols and the numerical simulations of Hazel & Heil (2006) are plotted using lines. These correspond to steady solutions of the three-dimensional fully coupled fluid–structure interaction problem calculated in the limit of zero gravity using a finite-element method. The choice of zero gravity yielded symmetries about the principal axes of the cross-section, so that the computational domain could be reduced to a quarter of this cross-section over a chosen length of tube. The numerical computations were performed using the code described by Hazel & Heil (2006) for

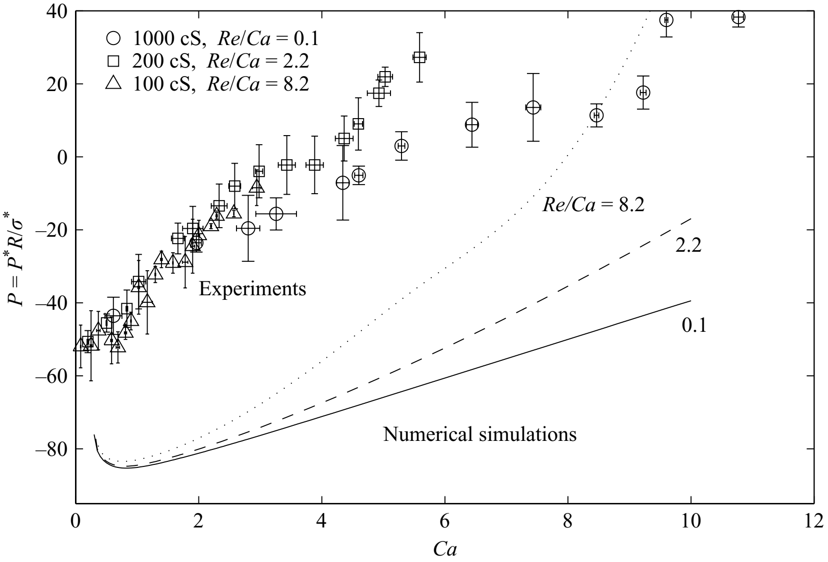

FIGURE 9. Comparison between the experimental and numerical bubble-pressure dependences on Ca for $Re/Ca = 0.1$, 2.2 and 8.2. The experimental measurements are plotted with symbols and the numerical results, computed with the code of Hazel & Heil (2006) for $A_\infty = 0.33$, $\sigma = 3.6 \times 10^{-2}$ and $h/R = 0.09$, are plotted with lines. The experimental variation in Re/Ca was achieved by using silicone oils of different viscosities (see table 1). The experimental results are averaged over the flow-rate values from 47 experiments at $Re/Ca = 0.1$, 111 experiments at $Re/Ca = 2.2$ and 74 experiments at $Re/Ca = 8.2$. The error bars correspond to the standard deviations of each group of data.

experimental parameter values $A_\infty = 0.33$, $\sigma = 3.6 \times 10^{-2}$ and $h/R = 0.09$. The Poisson ratio was set to 0.49 in the calculations, which is suitable for silicone as it is nearly incompressible.

In the experiment the range of attainable finger velocities was limited, since the maximum achievable flow rate was 1400 $\mathrm{cm^3\,min^{-1}}$. Thus, the maximum experimental capillary number varied from $Ca = 5.6$ for the 200 cS oil down to $Ca = 2.9$ for the 100 cS oil. For the 1000 cS oil the maximum flow rate investigated was 550 $\mathrm{cm^3\,min^{-1}}$, which limited the capillary-number range to $Ca \leqslant 11$. It is clear from all three sets of experimental data that the bubble pressure exhibits an overall growth with Ca, so that the tube is inflated with increasing driving force. Note that negative bubble pressures are recorded for $Ca < 4$, indicating that an air finger can ‘partially reopen’ a tube, so that its pressure remains less than the external pressure, as suggested by Hazel & Heil (2003). We shall further show in § 3.2.1 that in our experiments the tube never actually reaches its fully reopened cross-sectional area, estimated from the ‘tube law’, and remains partially buckled even for positive bubble pressures.

For $Ca \lesssim 3$, the experimental bubble pressure P does not exhibit a measurable dependence on Re/Ca but, for larger Ca, P exhibits steeper growth with Ca for $Re/Ca = 2.2$ than for $Re/Ca = 0.1$. Similarly, in the numerical simulations, when $Ca \leqslant 3.2$ the difference in pressure between $Re/Ca = 0.1$ and 8.2 is within the magnitude of the experimental uncertainty. For $Ca > 3.2$ the steepening of the pressure curves due to inertia as Ca increases results in a growing divergence between the values of the bubble pressure at a given Ca.

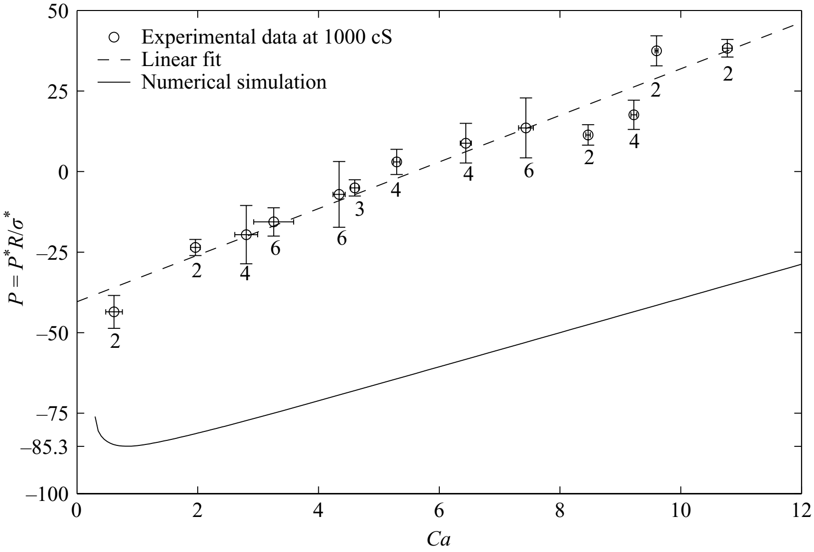

FIGURE 10. Bubble-pressure dependence on Ca for $Re/Ca = 0.1$. The number of experiments performed for each flow rate is indicated next to the experimental data points on the graph. The dashed line is a least-squares fit to the experimental data and the solid line represents the numerical results for $A_\infty = 0.33$ and $\sigma = 3.6 \times 10^{-2}$.

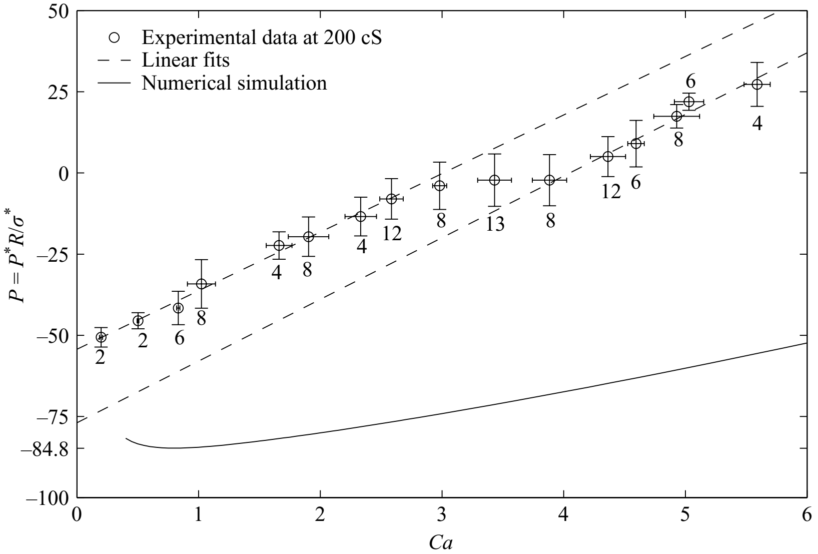

FIGURE 11. Bubble-pressure dependence on Ca for $Re/Ca = 2.2$. The number of experiments performed for each flow rate is indicated next to the experimental data points on the graph. The dashed line is a least-squares fit to the experimental data and the solid line represents the numerical results for $A_\infty = 0.33$ and $\sigma = 3.6 \times 10^{-2}$.

The pressure curves shown collectively in figure 9 are presented individually in figures 10, 11, 12 for $Re/Ca = 0.1$, 2.2 and 8.2 respectively. The number of experiments performed at each flow rate is indicated next to each data point on the graphs.

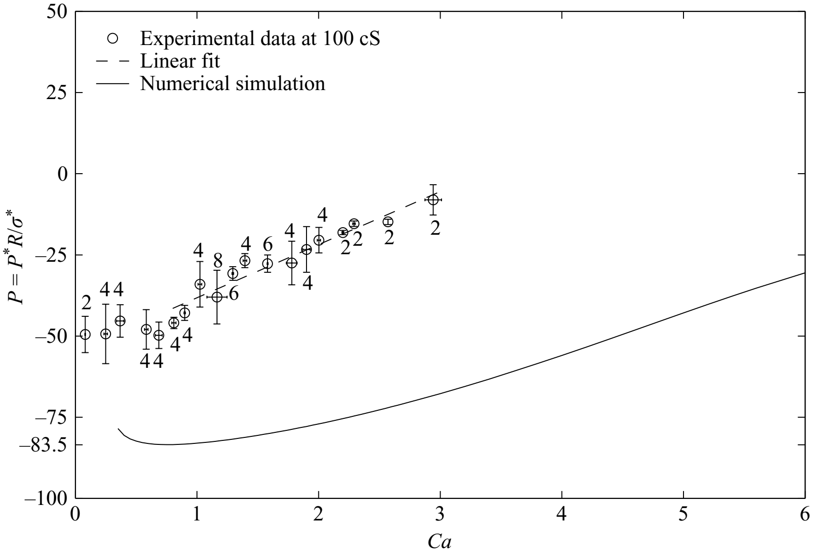

FIGURE 12. Bubble-pressure dependence on Ca for $Re/Ca = 8.2$. The number of experiments performed for each flow rate is indicated next to the experimental data points on the graph. The dashed line is a least-squares fit to the experimental data and the solid line represents the numerical results for $A_\infty = 0.33$ and $\sigma = 3.6 \times 10^{-2}$.

The three sets of experimental data exhibit significant qualitative differences. For $Re/Ca = 0.1$ (figure 10), the pressure increases approximately linearly, with a least-squares-fitted slope $\mathrm{d}P/\mathrm{d}Ca = 7.2 \pm 1.0$. For $Re/Ca = 2.2$ (figure 11), a linear increase is followed by a region of constant and approximately zero average bubble pressure between $Ca = 3.0$ and 3.9, with a subsequent linear increase for $Ca > 3.9$. A large number of experiments (111) was performed in this case to resolve the nonlinear dependence of the pressure on Ca. Least-squares fits to the regions of linear increase yield similar slopes: $\mathrm{d}P/\mathrm{d}Ca = 18.0 \pm 1.0$ for $Ca \leqslant 2.6$ and $\mathrm{d}P/\mathrm{d}Ca = 19.0 \pm 2.9$ for $Ca \geqslant 4.4$, while the average slope of the bubble-pressure curve over the experimental range of Ca investigated is approximately 15.4. In addition, small-amplitude periodic pressure oscillations (with approximate period 0.3 s) were reproducibly detected for $3.0 \leqslant Ca \leqslant 3.9$, where the averaged pressure remained constant. These may indicate the existence of a transition region between two steady 'peeling' states. Owing to the limited Ca range over which the oscillations occurred, as well as their small amplitude, the unexpected qualitative features of the pressure curve could not be investigated in further detail. The existence of the constant-pressure region, however, is confirmed by independent measurements presented in § 3.2.2. Finally, for $Re/Ca = 8.2$ (figure 12), the pressure remains approximately constant for $Ca < 0.8$. Indeed, for flow rates between 50 and 250 $\mathrm{cm}^3\,\mathrm{min}^{-1}$, similar bubble pressures were measured while the speed of the air finger underwent a tenfold increase. For $Ca > 0.8$, the pressure grows approximately linearly, with a least-squares-fitted slope $\mathrm{d}P/\mathrm{d}Ca = 16.4 \pm 2.6$ within the limited range of Ca attainable.

In the limit of small Ca, the experimental bubble pressure P shown in figure 9 tends to a value of about −50 in all three experiments, which is considerably lower than the yield pressure measured by Gaver III *et al.* (1990) in a tube of negligible bending stiffness. This result emphasizes the importance of the bending stiffness in determining the yield pressure. The region of minimum bubble pressure in the numerical simulations

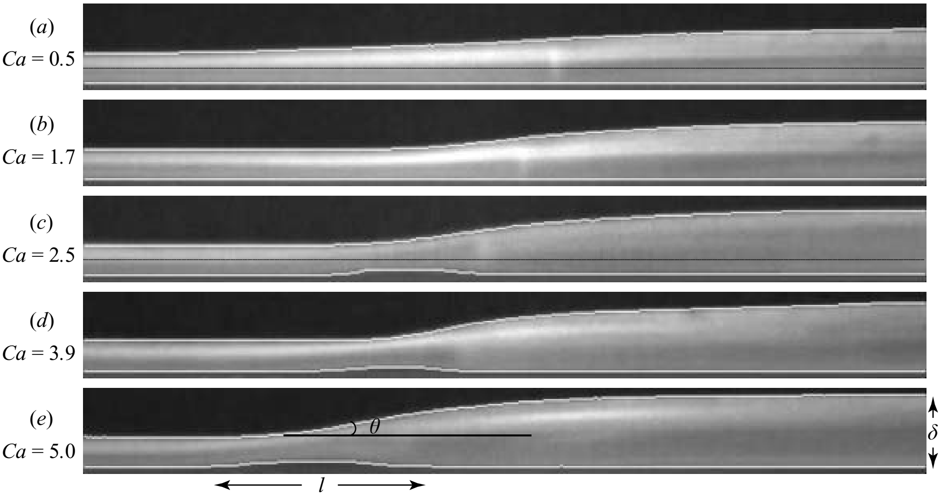

FIGURE 13. A series of side-view snapshots of reopening tubes filled with 200 cS oil, for increasing capillary numbers between $Ca = 0.5$ and 5.0. The horizontal solid lines in (*a*) and (*c*) denote the horizontal mid-plane far ahead of the finger tip and illustrate the asymmetry in the reopening tube. The outline of each tube is digitally traced (the white solid lines), in order to extract quantitative measures from the images: δ, the height of the reopened tube; θ, the upper-surface reopening angle; l, the length of tube which has lifted off the bottom rigid support, as shown in (*e*). The height of each snapshot is 10.9 mm.

marks the transition between the 'pushing' regime, where the pressure decreases with Ca and the air finger displaces a plug of fluid ahead of its tip, and the 'peeling' regime, where the pressure increases with Ca (Hazel & Heil 2003). The minimum pressure predicted by the computations remains approximately constant, at between −85.3 and −83.5 for increasing Re/Ca, which is smaller than the experimental minimum pressure by a factor of approximately 1.7. In the limit of small σ, the numerical calculations of Hazel & Heil (2003) showed that the reopening pressure varies significantly with σ. The effect of the experimental error in $\sigma = (3.6 \pm 0.2) \times 10^{-2}$ was assessed by performing calculations for the maximum and minimum experimental values of σ respectively. The resulting numerical pressure curves are shifted up and down by approximately six units on the capillary scale, which is insufficient to explain the discrepancy between the experimental and numerical pressures. The results of Jensen *et al.* (2002), however, show that at small Ca the pressure of a bubble reopening a channel asymmetrically is a factor of approximately 1.6 larger than in the symmetric configuration. This increase in the reopening pressure is likely to be due to the reduced radius of curvature at the interface, which in turn increases the pressure difference, causing adhesion. In the present experiments, we also observed asymmetric reopening configurations which arise owing to the coupling of gravity with elastic forces, which determines the tube's overall shape, as discussed in § 3.2. Thus, we speculate that the quantitative difference between the experimental and numerical reopening pressures originates in the gravity-induced asymmetric reopening configurations observed experimentally (see figure 13).

Also, the increasing length of the transition region between the collapsed and reopened regions of the tube, visible in figure 13 for decreasing Ca, is suggestive of the existence of a 'pushing' regime in the experiments. For $Re/Ca = 8.2$, where detailed data was sampled in the limit of small Ca, the saturation of the pressure for small Ca could further indicate the vicinity of a 'pushing' branch. The recent theoretical results of Halpern *et al.* (2005) support this notion as they demonstrate that at a constant, low, flow rate, steady pushing behaviour, although unstable, may be experimentally realizable for a significant period of time, at least until the bubble has advanced far enough for the compliance of the inflated section to destabilize the pushing motion.

The large discrepancy between experimental and numerical minimum pressures is accompanied by a discrepancy in the rate of growth of the bubble pressure with Ca. The average rates of growth of the numerical bubble pressure over the experimental ranges of Ca are $\mathrm{d}P/\mathrm{d}Ca = 5.2$, 6.6 and 9.2 for $Re/Ca = 0.1$, 2.2 and 8.2, respectively. Thus, the net effect of inertia is small over this limited range of Ca. The much larger increase in growth rates from $\mathrm{d}P/\mathrm{d}Ca = 7.2$ for 1000 cS oil to $\mathrm{d}P/\mathrm{d}Ca = 15.4$ and $\mathrm{d}P/\mathrm{d}Ca = 16.4$ for 200 cS and 100 cS oils, respectively, suggests that in the presence of gravity the reduction in the viscosity has additional consequences which dominate over the purely inertial pressure steepening.

3.2. *Effect of gravity on the reopening dynamics*

The differences between the experiments and the simulations appear to be closely linked to the presence of gravity in the experiment. Because of gravity, a rigid plate is necessary to support the bottom boundary of the reopening tube in the experiments, which leads to asymmetrical reopening of the tube, to be discussed in § 3.2.2. The second effect of gravity is to induce buoyancy pressures inside the tube. Experimentally, we observe that the steadily propagating air finger is located toward the top of the tube, so that the liquid film left behind on the walls of the tube is thicker below the finger. Evidence presented in § 3.2.1 suggests that the relative importance of gravity compared with inertia, enhanced through the increase in viscosity, is the key to determining the shape of the reopened tube far behind the finger tip.

A series of side-view snapshots of reopening tubes, filled with 200 cS oil, is shown in figure 13 for values of the capillary number Ca between 0.5 and 5.0. The air finger is propagating from the right to the left of each picture (i.e. from the reopened air-filled tube to the collapsed liquid-filled tube). The consecutive snapshots indicate that the height of the reopened tube increases with Ca, in accord with the pressure measurements presented in § 3.1. Also, the transition region between the uniformly collapsed tube and the uniformly reopened tube shortens significantly with increasing Ca. Both these findings were observed in the numerical simulations of Hazel & Heil (2003). A closer inspection of the images in figure 13, however, reveals that the experimentally reopened tube is inherently asymmetric about the horizontal mid-plane far ahead of the finger tip, as illustrated in snapshots (*a*) and (*c*), where the black horizontal line denotes the mid-plane. For small values of Ca (figure 13*a*, *b*), the tube lies flat on the rigid base and the deformation of the tube between the collapsed and reopened states is characterized solely by the upper-surface reopening angle θ. For $Ca > 2.0$, the tube lifts off the bottom plate over a length l, thus reducing the asymmetry in the transition region. A Matlab program was developed to extract quantitative measures from the snapshots. Firstly, an edge-finding algorithm was applied to trace digitally the outline of the tube (the solid white lines in figure 13). The contour data was then used to extract the quantitative measures illustrated in figure 13(*e*): δ is the height of the reopened tube; l is the length of tube which has lifted off the rigid plate and θ is the upper-boundary reopening angle. The angle θ was determined by calculating the average slope of the upper boundary in the transition region. Group averages of θ, l and δ were calculated for each value of the flow rate,

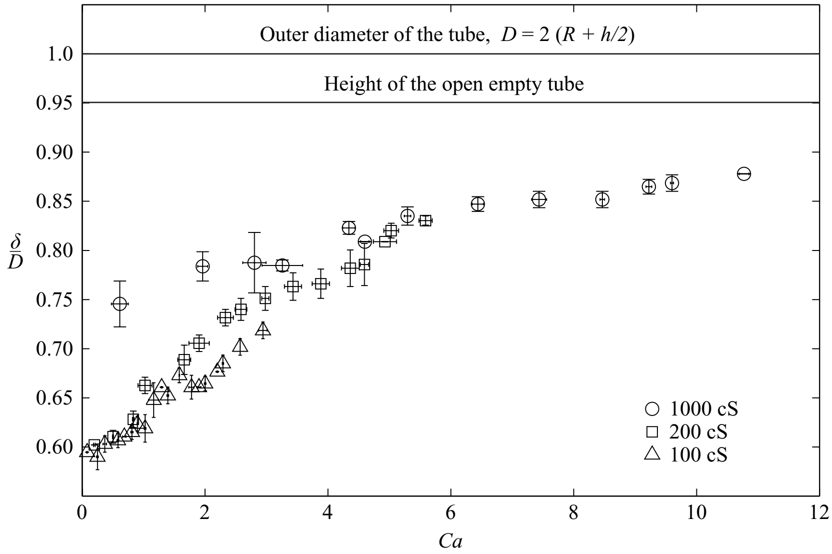

FIGURE 14. Dependence of the height of the reopened tube on Ca. The initial height of the collapsed tube is 3.69 mm, i.e. $\delta/D = 0.34$, where $D = 2(R + h/2)$ is the outer diameter of the tube. The upper and lower thick horizontal lines represent the outer diameter and the *in-situ* height of the open empty tube, respectively.

with upper and lower error estimates equal to one standard deviation about the mean data.

3.2.1. *The reopened tube behind the propagating air finger*

We begin by presenting the scaled height of the reopened tube δ/D against Ca in figure 14. The scaling factor, $D = 2(R + h/2) = 10.7$ mm, corresponds to the outer diameter of the tube. The upper thick horizontal line on the graph is for $\delta/D = 1.0$ and is approximately equal to the height expected in the zero-gravity fluid-filled configuration for $P = 0$. The effect of gravity on the open empty tube is to reduce its height by approximately 5 %, as indicated by the lower horizontal line. Over the range of Ca investigated, the reopening height appears to saturate at approximately $\delta/D = 0.89$, which is 7 % less than the height of empty tube at $P = 0$ in the experiment. For the 100 cS and 200 cS oils, δ/D grows faster with Ca than for the 1000 cS oil. This trend is expected from the behaviour of the pressure with Ca (see figure 9). With $Bo = 12.1$, viscous forces become comparable to buoyancy forces as Ca increases; $Ca/Bo = 0.9$ for the largest value reached by Ca in the experiment. Thus, the height measurements taken with oils of different viscosities tend to a similar value as Ca increases.

An unexpected result, however, is that for small values of Ca the tube reopens to larger heights with 1000 cS oil than with the lower-viscosity fluids, with up to 10 % difference between the reopening heights at 100 cS and 1000 cS even though the bubble pressure does not exhibit a measurable dependence on viscosity for $Ca \lesssim 3$, as shown in figure 9. The height of reopening, however, is linked to the distribution of the transmural pressure within the tube. Even when the bubble pressure remains constant, the transmural pressure distribution may be non-uniform and may vary through changes in the liquid film configurations, which result in different load distributions on the tube walls and thus in variations in the height of reopening. The

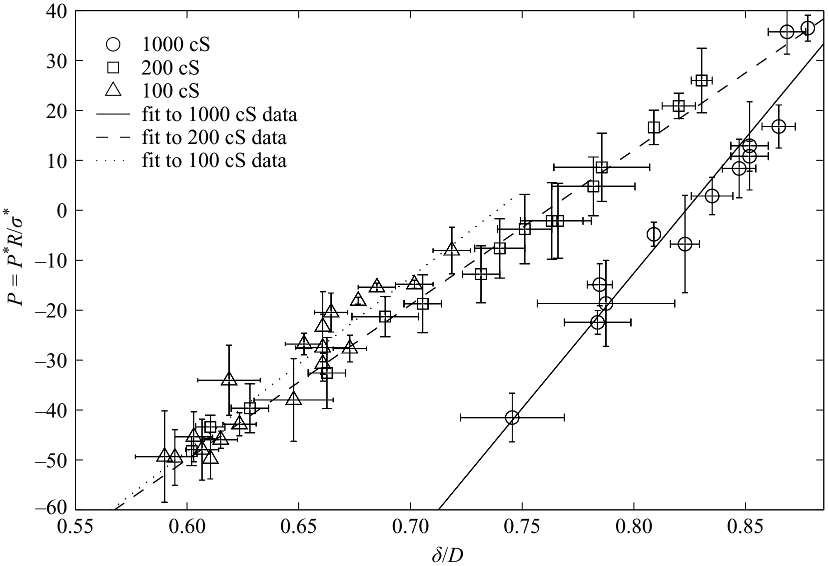

FIGURE 15. Modified experimental 'tube law' for the liquid-lined configuration: the dimensionless pressure of reopening, P, is plotted against the scaled height of the reopened tube, δ/D, where $D = 2(R + h/2)$ is the outer diameter of the tube, for all three values of viscosity investigated.

ratio of buoyancy and viscous forces, Bo/Ca, depends on the viscosity only through Ca. The ratio of buoyancy and inertial forces, $Bo/(Ca\,Re)$, however, is proportional to the square of the dynamic viscosity at a given Ca value, so that when $Ca = 0.5$, $Bo/(Ca\,Re) \simeq 5.9$, 22 and 539, for the 100 cS, 200 cS and 1000 cS oils respectively. Given the variation by a factor 100 in $Bo/(Ca\,Re)$, it is likely that the competition between buoyancy and inertial forces in the experiment results in widely different film configurations, particularly in the 1000 cS experiments, compared with the other two cases.

In addition, for the 100 cS and 200 cS oils, the reopened height did not vary after the passage of the bubble on the time scale of the experiment. For 1000 cS, a minor reduction in δ of less than 5 % was detected, which may indicate the redistribution of the load on the tube walls through drainage. Indeed, in the presence of gravity, the final film configuration is only expected to be reached at very large times, because of the increasing time scales associated with the drainage of thin liquid films left on the tube walls after the passage of the bubble. The experimental evidence, however, suggests that the effect of drainage on δ is very small for the grades of silicone oil investigated.

To demonstrate further the dependence of the scaled reopening height on viscosity, P is plotted against δ/D in figure 15 for the three values of viscosity investigated. The pressure-versus-scaled-height data is approximately linear within the experimental range investigated, suggesting the proportional growth of both quantities. The significantly different slope of the $(P, \delta/D)$-curve for the 1000 cS oil compared to those for the 100 and 200 cS oils confirms that different heights of reopening can occur for the same bubble pressure, depending on the viscosity of the liquid used in the experiment. Thus when $P = 0$, for instance, the height of reopening increases monotonically with increasing viscosity. We were also able to reproduce this result

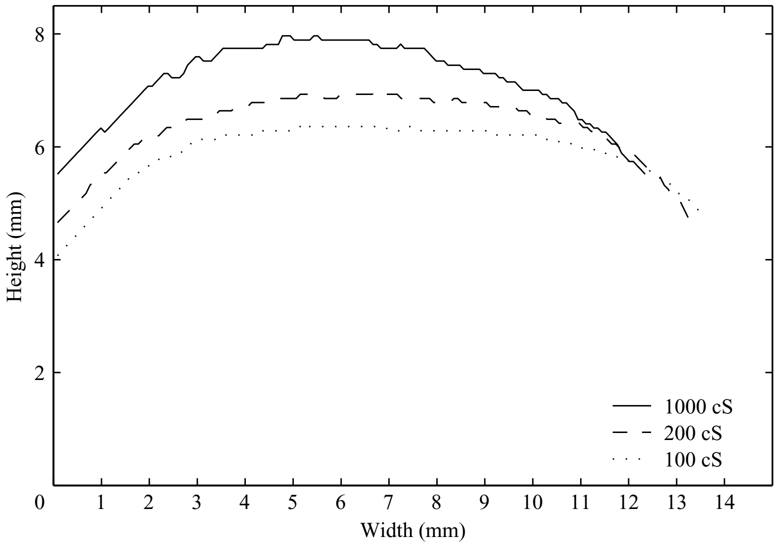

FIGURE 16. Outline of the top section of the reopened tube measured with the aerial camera for 1000 cS, 200 cS and 100 cS silicone oil at $P = -44 \pm 1$.

independently by measuring the height of the fluid-filled reopened tubes from the video footages recorded at $50\,\mathrm{cm}^3\,\mathrm{min}^{-1}$, once the reopening experiment was over and the end two-way valve had been released to let air flow through the system.

In figure 16 a further comparison may be made of the outline of the tube captured by the aerial camera for different-viscosity oils, at a constant bubble pressure $P = -44 \pm 1$. The curves were obtained by digitally tracing the deformed laser line outlining the upper section of the reopened tube in the aerial view snapshots (see figure 2). These results clearly demonstrate that the shape of the cross-section, as well as its height, are strongly dependent on viscosity, with increasingly reopened tubes observed for larger-viscosity oils. Note that all the reopened tube profiles exhibit a small asymmetry about the mid-width of the tube. This asymmetry is linked to the manufacturing process of the silicone tubing, where a large piece of solid silicone is extruded into a coil, resulting in slightly curved tubes with a natural transverse distortion of less than 3 % of their length.

3.2.2. *The transition region of the reopening tube*

In figure 17, the angle of reopening, θ, and the length of lift-off, l, are plotted against Ca for each value of viscosity. The upper reopening angles are shown in the left-hand column, while the length of lift-off is plotted in the right-hand column. Figures 17(*a*), (*b*) are for the 1000 cS silicone oil, figures 17(*c*), (*d*) are for the 200 cS silicone oil and figure 17(*e*) is for the 100 cS silicone oil. Starting with figures 17(*c*), (*d*), the angle of reopening grows approximately linearly up to $Ca \simeq 1.9$ and, within this range, the tube does not lift off the base plate. The onset of lift-off occurs between $Ca = 1.7$ and $Ca = 1.9$, and l then grows linearly up to $Ca \simeq 3.0$, which is the lower bound for the region of constant pressure seen in figure 11. The upper-surface reopening angle remains constant within this range of Ca. For $3.0 \lesssim Ca \lesssim 3.9$, which corresponds to the region of constant pressure, the trend reverses so that θ grows linearly while l remains constant, and vice versa for $Ca \gtrsim 3.9$. Hence, in the 200 cS experiments, successive phases in the reopening process are identified which are dominated by

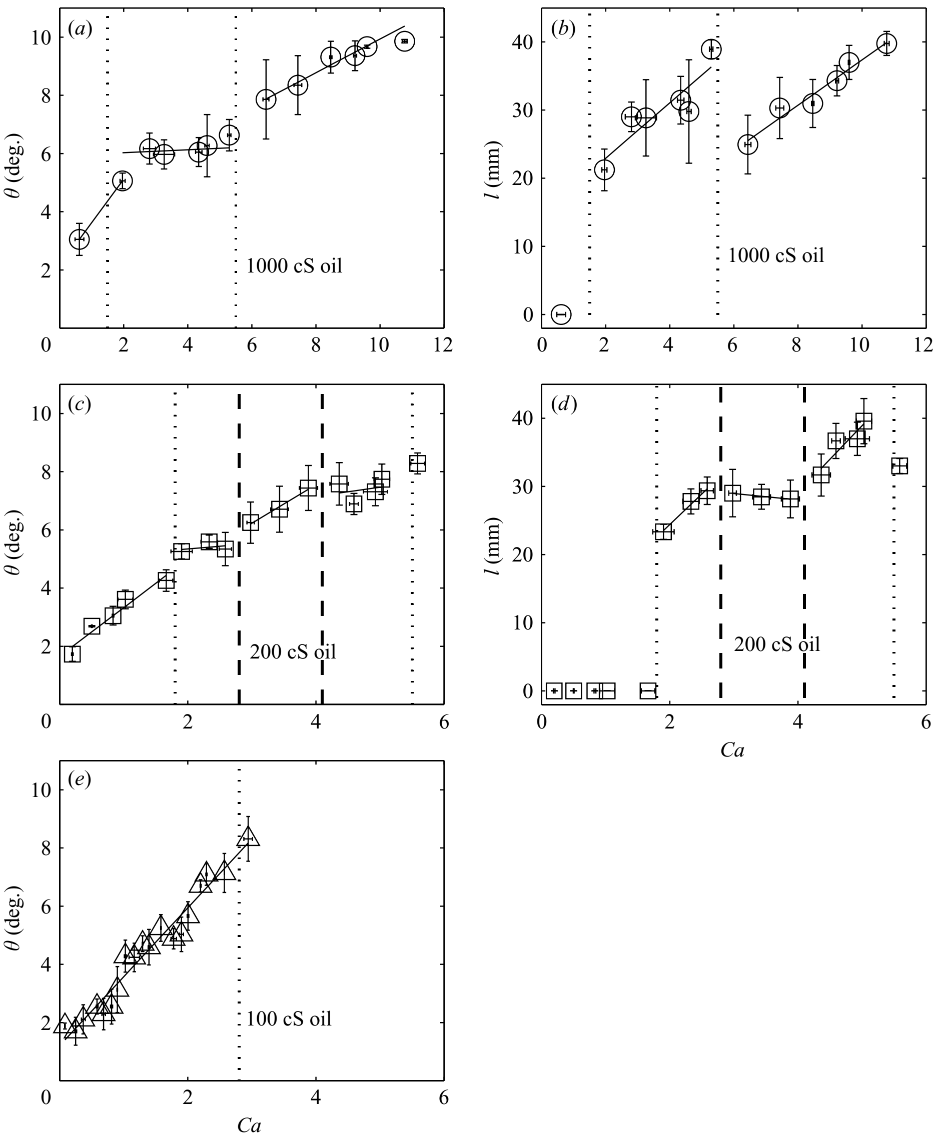

FIGURE 17. Correlation between the angle of reopening, θ (left-hand column) and the length of lift-off, l, (right-hand column): (*a*), (*b*) 1000 cS oil; (*c*), (*d*) 200 cS oil; (*e*) 100 cS oil. In the last case, lift-off was detected only at the largest achievable value of Ca, 2.9, and thus the dependence of l on Ca is not shown. The solid lines are local linear fits to the data, which have been plotted as a guide to the eye. The vertical dotted lines in (*a*)–(*d*) give the approximate value of Ca for which lift-off first occurs (left-hand line), and beyond which the length of lift-off is observed suddenly to drop (right-hand line). The vertical dashed lines in (*c*) and (*d*) delimit the range of Ca where a constant bubble pressure of approximately zero is observed.

the deformation of either the upper or lower boundary of the tube. In figures 17(*a*), (*b*), which are for 1000 cS oil, lift-off again does not occur for small values of Ca, and θ increases sharply for $Ca \lesssim 2.0$. The lift-off occurs between $Ca = 0.6$ and $Ca = 2.0$, but the sparse measurements at low Ca in this case do not allow us to resolve the threshold further. This is followed by a region of approximately constant

θ (slow growth), with significant growth of l for $2.0 \lesssim Ca \lesssim 5.3$. As in the case of the 200 cS oil, this indicates the successive phases of reopening with Ca. There does not appear to be any additional feature in the angle and length of lift-off for $2.0 \lesssim Ca \lesssim 5.3$, in accord with the pressure results shown in figure 10, although the smaller number of experiments (47) performed with this viscosity grade and the wider range of Ca covered do not permit us to ascertain this conclusively. For $Ca = 6.4$, l drops sharply from approximately 38 mm to 24 mm. For $Ca \gtrsim 6.4$, it resumes linear growth, and θ also sharply increases. This indicates a rearrangement of the transition region of the tube, which appears to occur at a critical value of Ca. Evidence for this behaviour is also seen in figures 17(*c*), (*d*) for $Ca = 5.6$ (the last experimental point). Finally, in the 100 cS experiments, lift-off is delayed, as we detected it only in the last experimental measurement at $Ca = 2.9$. Thus, we show only the variation in θ with Ca in figure 17(*e*). It appears to increase in an approximately linear manner, similarly to the pressure presented in figure 12. The angle of reopening, however, does not appear to saturate in the limit of small Ca, indicating that evolution of the transition region is significant even in the initial constant-pressure region ($Ca < 0.8$).

The different configurations of the transition region described above for increasing Ca are a consequence of the gravity-induced asymmetry of the reopening tube. Note that such features are not expected in the model of Hazel & Heil (2003, 2006), where symmetries about the principal axes of the cross-section are enforced.

4. Conclusion

The results of an experimental investigation into the mechanics of airway reopening have been presented. The injection of nitrogen at a constant flow rate into a liquid-filled collapsed tube of finite bending stiffness resulted in the steady propagation of an air finger after initial transients had decayed. We have demonstrated that gravity has a profound effect on the reopening mechanics and is closely linked to the significant differences from the three-dimensional zero-gravity model of Hazel & Heil (2006). The ratio of gravity and inertial forces increases as the square of the viscosity of the liquid for a given value of Ca. Thus, an increase in viscosity yields changes in the film configuration behind the propagating finger, which in turn alters the mechanical load on the tube walls. As a result, differing tube heights and cross-sectional shapes are found for different values of the viscosity at the same bubble pressure. The presence of gravity also requires the tube to be supported, and this induces an asymmetry about the horizontal mid-plane. The different phases of reopening observed for increasing Ca are linked to this asymmetry. In order to avoid the need for a rigid support plate, the experiments could conceivably be carried out by immersing the tube in silicone oil. Because of buoyancy, however, the reopening fluid would also need to be density-matched to silicone oil, and significant practical difficulties would be associated with this setup.

The liquid lining in a healthy lung has a viscosity $\mu \simeq 10^{-3}\ \mathrm{kg\,m^{-1}\,s^{-1}}$ (Kamm & Schroter 1989), which is much lower than in the experiments. Thus with $Ca = 0.05$, which corresponds to propagation speeds of $1\ \mathrm{m\,s^{-1}}$ in the lungs (Halpern, Jensen & Grotberg 1998), and considering the smallest airways of radius 0.29 mm (Kamm & Schroter 1989), we have $Bo/(Ca\,Re) \simeq 3 \times 10^{-3}$, which suggests that buoyancy will have a minimal influence on the dynamics. Mucous secretions in a diseased lung can, however, result in viscosities equal to the lowest value investigated in the experiment, $\mu = 10^{-1}\ \mathrm{kg\,m^{-1}\,s^{-1}}$ (Gaver III, Samsel & Solway 1990). In this case, the relative importance of buoyancy could be significantly increased. For potentially smaller propagation speeds, of the order of $10^{-2}\,\mathrm{m\,s^{-1}}$, inertial forces become negligible and the relevant force balance, Bo/Ca, is approximately 82 in the healthy lung and 0.8 in the diseased lung, suggesting that gravity may significantly influence the reopening process. Finally, the bending stiffness in the experiments is approximately a factor 10^2 larger than in the terminal bronchioles of the lungs, whereas the radius of the tube is approximately 16 times that of these airways. A typical value for the ratio of surface tension and bending forces in the lung is $\sigma = 50$ (Hazel & Heil 2003), which may be compared with $\sigma = 3.6 \times 10^{-2}$ in the experiment. Thus, the ratio of gravity and elastic forces, $Bo\sigma = \rho g R/K$ is approximately equal to 0.4 in the experiments, whereas it is 2 in the lungs. It is therefore likely that gravity may influence the reopening process in the lungs.

The authors wish to thank Dr M. Heil and Dr A. L. Hazel for kindly providing the numerical data shown in § 3.1 and for many useful discussions and valuable comments during the preparation of this manuscript. They also thank the three referees for their constructive comments, which have helped to improve the manuscript. This work was funded by the EPSRC (AH) and an EPSRC ‘Advanced Research Fellowship’ (AJ).

REFERENCES

Flaherty, J. E., Keller, J. B. & Rubinow, S. I. 1972 Post-buckling behaviour of elastic tubes and rings with opposite sides in contact. *SIAM J. Appl. Maths* **23**, 446–455.

Gaver III, D. P., Halpern, D., Jensen, O. E. & Grotberg, J. B. 1996 The steady motion of a semi-infinite bubble through a flexible-walled channel. *J. Fluid Mech.* **319**, 25–65.

Gaver III, D. P., Samsel, R. W. & Solway, J. 1990 Effects of surface tension and viscosity on airway reopening. *J. Appl. Physiol.* **69**, 74–85.

Grotberg, J. B. 2001 Respiratory fluid mechanics and transport processes. *Annu. Rev. Biomech. Eng.* **3**, 421–457.

Halpern, D. & Grotberg, J. B. 1992 Fluid-elastic instabilities of liquid-lined flexible tubes. *J. Fluid Mech.* **244**, 615–632.

Halpern, D., Jensen, O. E. & Grotberg, J. B. 1998 A theoretical study of surfactant and liquid delivery into the lung. *J. Appl. Physiol.* **85**, 333–352.

Halpern, D., Naire, S., Jensen, O. E. & Gaver III, D. P. 2005 Unsteady bubble propagation in a flexible channel: predictions of a viscous stick-slip instability. *J. Fluid Mech.* **528**, 53–86.

Hazel, A. L. & Heil, M. 2003 Three-dimensional airway reopening: The steady propagation of a semi-infinite bubble into a buckled elastic tube. *J. Fluid Mech.* **478**, 47–70.

Hazel, A. L. & Heil, M. 2005 Surface-tension-induced buckling of liquid-lined elastic tubes: a model for pulmonary airway closure. *Proc. R. Soc. A* **461**, 1847–1868.

Hazel, A. L. & Heil, M. 2006 Finite Reynolds number effects in steady, three-dimensional airway reopening. *Trans. ASME: J. Biomech. Engng* **128**, 473–478.

Heil, M. 2000 Finite Reynolds number effects in the propagation of an air finger into a liquid-filled flexible-walled channel. *J. Fluid Mech.* **424**, 21–44.

Jensen, O. E., Horsburgh, M. K., Halpern, D. & Gaver III, D. P. 2002 The steady propagation of a bubble in a flexible-walled channel: asymptotic and computational models. *Phys. Fluids* **14**, 443–457.

Kamm, R. D. & Schroter, R. C. 1989 Is airway closure caused by a liquid film instability? *Resp. Physiol.* **75**, 141–156.

Low, H., Chew, Y. & Zhou, C. 1997 Pulmonary airway reopening: effects of non-Newtonian fluid viscosity. *Trans. ASME: J. Biomech. Engng* **119**, 298–308.

Macklem, P. T., Proctor, D. F. & Moss, J. C. 1970 The stability of peripheral airways. *Resp. Physiol.* **8**, 191–203.

Naire, S. & Jensen, O. 2005 Epithelial cell deformation during surfactant-mediated airway reopening: a theoretical model. *J. Appl. Physiol.* **99**, 458–471.

Naureckas, E. T., Dawson, C. A., Gerber, B. S., Gaver III, D. P., Gerber, H. L., Lineran, J. M., Solway, J. & Samsel, R. W. 1994 Airway reopening pressure in isolated rat lungs. *J. Appl. Physiol.* **76**, 1372–1377.

Perun, M. L. & Gaver III, D. P. 1995*a* An experimental model investigation of the opening of a collapsed untethered pulmonary airway. *Trans. ASME: J. Biomech. Engng* **117**, 245–253.

Perun, M. L. & Gaver III, D. P. 1995*b* Interaction between airway lining fluid forces and parenchymal tethering during pulmonary airway reopening. *J. Appl. Physiol.* **79**, 1717–1728.

Schatz, M. F., VanHook, S. J., McCormick, W., Swift, J. B. & Swinney, H. L. 1995 Onset of surface-tension-driven Bénard convection. *Phys. Rev. Lett.* **75**, 1938–1941.

Shapiro, A. H. 1977 Steady flow in collapsible tubes. *Trans. ASME: J. Biomech. Engng* **99**, 126–147.

White, J. P. & Heil, M. 2005 Three-dimensional instabilities of liquid-lined elastic tubes: A thin-film fluid-structure interaction model. *Phys. Fluids* **17**, 031506.